41st Aerospace Sciences Meeting and Exhibit
6-9 January 2003, Reno, Nevada

AIAA 2003-0953

A Unified Boundary Treatment in Lattice Boltzmann Method

Dazhi Yu**, Renwei Mei*, and Wei Shyy†

Department of Mechanical and Aerospace Engineering
University of Florida, Gainesville, FL 32611-6250 USA

ABSTRACT

In the method of lattice Boltzmann equation, the distribution functions on curved solid boundary cannot be specified exactly. Among various approximate methods, one either treats the wall as a series of steps or employs a combination of different interpolations which are valid in their respective parameter ranges. In this paper, a unified treatment for the curved wall is presented. In the unified scheme, the value of the distribution function on the wall is first constructed based on the principle of momentum balance. A single interpolation is then used to obtain the desired distribution functions on the boundary lattice nodes. Results from several tests show that this scheme maintains the geometric integrity of curved wall and has a second order accuracy. It is robust and easy to implement.

1. BACKGROUND OF THE LATTICE BOLTZMANN METHOD

Recently, there has been much progress in developing and employing the method of the lattice Boltzmann equation (LBE) [1-3] as an alternative, non-traditional computational technique for solving complex fluid dynamic systems [4-5]. In an NS equation-based macroscopic method for computational fluid dynamics (CFD), the macroscopic variables of interest, such as velocity $\boldsymbol{u}$ and pressure p, are obtained by solving the Navier-Stokes (NS) equations [6-8]. In the LBE approach, one solves the kinetic equation for the particle mass distribution function $f(\boldsymbol{x},\boldsymbol{\xi},t)$ and the macroscopic quantities (such as mass density ρ and momentum density $\rho\boldsymbol{u}$) can then be obtained by evaluating the hydrodynamic moments of the distribution function f.

A popular kinetic model is the Boltzmann equation with the single relaxation time approximation [9]:

$$\frac{\partial f}{\partial t}+\boldsymbol{\xi}\cdot\nabla f = -\frac{1}{\lambda}(f-f^{(eq)}) \tag{1}$$

where $\boldsymbol{\xi}$ is the particle velocity, $f^{(eq)}$ is the equilibrium distribution function (the Maxwell-distribution function), and λ is the relaxation time. The viscosity is $\nu=\lambda c_s^2$ in which c_s is the speed of sound.

To solve for f numerically, Eq. (1) is first discretized in the velocity space $\boldsymbol{\xi}$ using a finite set of velocities $\{\boldsymbol{\xi}_\alpha\}$ in the context of the conservation laws [5, 9-11],

$$\frac{\partial f_\alpha}{\partial t}+\boldsymbol{\xi}_\alpha\cdot\nabla f_\alpha = -\frac{1}{\lambda}(f_\alpha-f_\alpha^{(eq)}) \tag{2}$$

In the above, $f_\alpha(\boldsymbol{x},\ t)\equiv f(\boldsymbol{x},\ \boldsymbol{\xi}_\alpha,\ t)$ is the distribution function associated with the direction $\boldsymbol{\xi}_\alpha$ and $f_\alpha^{(eq)}$ is the equilibrium distribution function of the α-th discrete velocity. The 9-bit (or 9-velocity) square lattice model, which is also called D2Q9 model (Fig. 1) has been widely used for simulating 2-D flows. For D2Q9 model, we use $\boldsymbol{e}_\alpha$ to denote the discrete velocity set

$$\begin{aligned}&\boldsymbol{e}_0 = 0,\\ &\boldsymbol{e}_\alpha = c\,(\cos((\alpha-1)\pi/4),\sin((\alpha-1)\pi/4)) \quad \text{for } \alpha=1,3,5,7,\\ &\boldsymbol{e}_\alpha = c\sqrt{2}(\cos((\alpha-1)\pi/4),\sin((\alpha-1)\pi/4)) \quad \text{for } \alpha=2,4,6,8\end{aligned} \tag{3}$$

where $c=\delta x/\delta t$, δx and δt are the lattice constant and the time step size, respectively. The equilibrium distributions for D2Q9 model (as well as for some of the 3-D lattice models) are in the form of

$$f_\alpha^{(eq)} = \rho w_\alpha\left[1+\frac{3}{c^2}\boldsymbol{e}_\alpha\cdot\boldsymbol{u}+\frac{9}{2c^4}(\mathbf{e}_\alpha\cdot\boldsymbol{u})^2-\frac{3}{2c^2}(\boldsymbol{u}\cdot\boldsymbol{u})^2\right] \tag{3}$$

where w_α is the weighting factor given by

$$w_\alpha=\begin{cases}4/9, & \alpha=0\\ 1/9, & \alpha=1,3,5,7\\ 1/36, & \alpha=2,4,6,8.\end{cases} \tag{4}$$

With the discretized velocity space, the density and mass flux can be evaluated as

$$\rho=\sum_{k=0}^{8}f_\alpha=\sum_{k=0}^{8}f_\alpha^{(eq)} \tag{5a}$$

and

$$\rho\boldsymbol{u}=\sum_{k=1}^{8}\boldsymbol{e}_\alpha f_\alpha=\sum_{k=1}^{8}\boldsymbol{e}_\alpha f_\alpha^{(eq)} \tag{5b}$$

** Graduate student, * Professor, Associate Fellow AIAA † Professor and Chair, Fellow AIAA.

The speed of sound of this model is $c_s = c/\sqrt{3}$ and the equation of state is that of an ideal gas,

$$p = \rho c_s^2 \tag{6}$$

Equation (2) can be further discretized in space and time. The completely discretized form of Eq. (1), with the time step δt and space step $\boldsymbol{e}_\alpha \delta t$, is:

$$f_\alpha(\boldsymbol{x}_i + \boldsymbol{e}_\alpha \delta t,\, t + \delta t) - f_\alpha(\boldsymbol{x}_i,\, t) = -\frac{1}{\tau}[f_\alpha(\boldsymbol{x}_i, t) - f_\alpha^{(eq)}(\boldsymbol{x}_i, t)] \tag{7}$$

where $\tau = \lambda/\delta t$, and $\boldsymbol{x}_i$ is a point in the discretized physical space. The above equation is the lattice Boltzmann equation [1-3] with Bhatnagar-Gross-Krook (BGK) approximation. The viscosity in the NS equation derived from Eq. (7) is

$$\nu = (\tau - 1/2) c_s^2 \delta t \tag{8}$$

The modification of viscosity (from $\nu = \lambda c_s^2$ for Eq. (1)) corrects for the truncation error in the discretization of Eq. (2) and makes formally the LBGK scheme a second order method for solving incompressible flows [10] & [11]. The positivity of the viscosity requires that $\tau > ½$. Equation (8) can be solved as:

collision step:

$$\tilde{f}_\alpha(\boldsymbol{x}_i, t) = f_\alpha(\boldsymbol{x}_i,\, t) - \frac{1}{\tau}[f_\alpha(\boldsymbol{x}_i, t) - f_\alpha^{(eq)}(\boldsymbol{x}_i,\, t)] \tag{9a}$$

streaming step:

$$f_\alpha(\boldsymbol{x}_i + \boldsymbol{e}_\alpha \delta t, t + \delta t) = \tilde{f}_\alpha(\boldsymbol{x}_i, t) \tag{9b}$$

where $\sim$ denotes the post-collision state of the distribution function. It needs to be emphasized that with such a splitting in the computational procedure, there is no need to store both $f_\alpha(\boldsymbol{x}_i,\, t + \delta t)$ and $f_\alpha(\boldsymbol{x}_i,\, t)$ during the computation. Information on one time level is sufficient for unsteady flow simulations. It is also noted that the collision step is completely local and the streaming involves no computation. Equation (9) is explicit, easy to implement, and straightforward to parallelize.

In general, the boundary condition for the velocity at a solid wall is specified while the values for f_α's are unknown. In the LBE method, the velocity condition can only be satisfied approximately through f_α's. In

Figure **2**, a curved wall separates the solid region from the fluid region. The lattice node on the fluid side of the boundary is denoted as $\boldsymbol{x}_f$ and that on the solid side is denoted as $\boldsymbol{x}_b$. The filled small circles on the boundary, $\boldsymbol{x}_w$, denote the intersections of the wall with various lattice links. The boundary velocity at $\boldsymbol{x}_w$ is $\boldsymbol{u}_w$. The fraction of an intersected link in the fluid region is Δ, that is:

$$\Delta = \frac{|\boldsymbol{x}_f - \boldsymbol{x}_w|}{|\boldsymbol{x}_f - \boldsymbol{x}_b|}, \qquad 0 \le \Delta \le 1. \tag{10}$$

The horizontal or vertical distance between $\boldsymbol{x}_b$ and $\boldsymbol{x}_w$ is $\Delta\delta x$ on the square lattice. Right after the collision step, $\tilde{f}_\alpha(\boldsymbol{x}_f)$ on the fluid side node $\boldsymbol{x}_f$ is known for all α, but $\tilde{f}_{\bar{\alpha}}(\boldsymbol{x}_b)$, the post-collision distribution function coming from $\boldsymbol{x}_b$ to $\boldsymbol{x}_f$, is not known. To complete the subsequent streaming step, $\tilde{f}_{\bar{\alpha}}(\boldsymbol{x}_b, t)$ is needed since it exactly gives $f_{\bar{\alpha}}(\boldsymbol{x}_f, t + \delta t)$ after streaming. A popular approach is to employ the bounce-back scheme [12][13]. In this scheme, the momentum from the incoming particle, $\tilde{f}_\alpha(x_f, t)\boldsymbol{e}_\alpha$, is bounced back in the opposite direction after the particle hits the wall. This scheme is intuitively derived from lattice gas automata [14] [15]. For a stationary wall, it is equivalent to setting $\tilde{f}_{\bar{\alpha}}(x_b, t) = \tilde{f}_\alpha(x_f, t)$. For a moving wall, a certain amount of momentum should be added to the bounced particle. This results in

$$\tilde{f}_{\bar{\alpha}}(x_b, t) = \tilde{f}_\alpha(x_f, t) + 2w_\alpha \rho_w \frac{3}{c^2} \boldsymbol{e}_{\bar{\alpha}} \cdot \boldsymbol{u}_w \tag{11}$$

for the bounce-back scheme with a moving wall where ρ_w is the fluid density at the wall, $\boldsymbol{u}_w$ is the wall velocity at $\boldsymbol{x}_w$. However, this is only a first order treatment in general [13]. Ziegler [12] made an improvement to the bounce-back at node scheme to the second order accuracy for non-slip condition on the wall. After streaming, $f_\alpha(\boldsymbol{x}_b)$ is known while $f_{\bar{\alpha}}(\boldsymbol{x}_b)$ is not known. After setting $f_{\bar{\alpha}}(\boldsymbol{x}_b) = f_\alpha(\boldsymbol{x}_b)$ on the wall (for the no-slip condition), an additional collision is then carried out at $\boldsymbol{x}_b$ to yield $\tilde{f}_{\bar{\alpha}}(x_b, t)$. This additional collision was responsible for the improved accuracy. In simulating suspension flow, Ladd [16] placed the wall halfway between the nodes with Δ=1/2. This method is referred to as bounce-back at link scheme. In doing so, the additional collision in Ziegler's scheme is avoided. It has been shown that this treatment has the second order accuracy for the straight wall. He *et al*. [22] also proved that bounce-back on the link scheme had second order accuracy for no-slip condition on the wall in a channel flow using analytical solution.

Nobel *et al*. [17] presented an improved boundary condition for 2-D hexagonal lattice. The hydrodynamic conditions, velocity and density at wall, were used to derived boundary condition for f_α's so that it can guarantee the no-slip condition. Inamuro *et al*. [18], and Maier *et al*. [19] subsequently presented similar schemes for square lattice to reduce the wall slip velocity. Chen *et al*. [20] placed the wall at the node and used extrapolation of f_α on the fluid side to obtain the f_α at $\boldsymbol{x}_b$. To solve f_α's which can satisfy hydrodynamic conditions at boundary nodes for D2Q9 and D2Q15 models, Zou and He [21] placed wall at nodes and extended the bounce-back scheme to the non-equilibrium part of distribution function.

All the boundary treatments mentioned above model curved wall as zig-zag steps, which results in geometric discontinuities and affects the computational accuracy. This error worsens when Re increases.

Filippova and Hänel [23] (hereinafter referred as to FH) presented a curved boundary condition which, for the first time, provided a second order accurate treatment for a curved solid wall. To improve the numerical stability, Mei *et al*. [24] presented an improved curved boundary condition based on FH's scheme. Bouzidi *et al*. [25] proposed a different but simpler boundary condition for curved wall based on interpolation and the bounce-back scheme. In order to establish the necessary background, these three treatments are briefly reviewed next.

To construct $\tilde{f}_{\bar{\alpha}}(\boldsymbol{x}_b,t)$ based on known information in the surrounding, FH [23] proposed the following linear interpolation:

$$\tilde{f}_{\bar{\alpha}}(\boldsymbol{x}_b,t)=(1-\chi)\,\tilde{f}_{\alpha}(\boldsymbol{x}_f,t)+\chi\, f_{\alpha}^{(*)}(\boldsymbol{x}_b,t)+2w_{\alpha}\rho\frac{3}{c^2}\,\boldsymbol{e}_{\bar{\alpha}}\cdot\boldsymbol{u}_w \qquad (12)$$

with

$$f_{\alpha}^{(*)}(\boldsymbol{x}_b,t)=w_{\alpha}\rho(\boldsymbol{x}_f,t)\,[1+\frac{3}{c^2}\boldsymbol{e}_{\alpha}\cdot\boldsymbol{u}_{bf}+\frac{9}{2c^4}(\boldsymbol{e}_{\alpha}\cdot\boldsymbol{u}_f)^2-\frac{3}{2c^2}\,\boldsymbol{u}_f\cdot\boldsymbol{u}_f] \qquad (13)$$

In the above, $\boldsymbol{u}_f\equiv\boldsymbol{u}(\boldsymbol{x}_f,t)$ is the fluid velocity near the wall and $\boldsymbol{u}_{bf}$ is to be chosen as

$$\boldsymbol{u}_{bf}=(\Delta\text{-}1)\boldsymbol{u}_f/\Delta+\boldsymbol{u}_w/\Delta \quad\text{and}\quad \chi=(2\Delta\text{-}1)/\tau \quad \text{for} \quad \Delta\geq 1/2 \qquad (14a)$$

$$\boldsymbol{u}_{bf}=\boldsymbol{u}_f \quad\text{and}\quad \chi=(2\Delta\text{-}1)/(\tau\text{-}1) \quad \text{for} \quad \Delta<1/2. \qquad (14b)$$

Equation (12) can be recast as follows:

$$\tilde{f}_{\bar{\alpha}}(\boldsymbol{x}_b,t)=\tilde{f}_{\alpha}(\boldsymbol{x}_f,t)-\chi[\tilde{f}_{\alpha}(\boldsymbol{x}_f,t)-f_{\alpha}^{(eq)}(\boldsymbol{x}_f,t)]+w_{\alpha}\rho(\boldsymbol{x}_f,t)\,\frac{3}{c^2}\boldsymbol{e}_{\alpha}\cdot(\boldsymbol{u}_{bf}-\boldsymbol{u}_f-\boldsymbol{u}_w) \qquad (15)$$

Thus, the above treatment of curved boundary can be thought as a modification of the relaxation (the viscous effect) near the wall (via parameter χ), in additional to a forcing term accounting for the momentum exchange effect due to the wall. Mei *et al*. [24] suggested using different nodes to obtain $\tilde{f}_{\bar{\alpha}}(\boldsymbol{x}_b,t)$ when $\Delta<0.5$. The purpose was to improve the numerical stability over FH's scheme. Thus, Eq. (14b) was replaced by

$$\boldsymbol{u}_{bf}=\boldsymbol{u}_{ff} \text{ and } \chi=(2\Delta\text{-}1)/(\tau\text{-}2) \quad \text{for} \quad \Delta<1/2 \qquad (16)$$

where $\boldsymbol{u}_{ff}=\boldsymbol{u}(\boldsymbol{x}_f+\boldsymbol{e}_{\alpha}\delta t)$ is the fluid velocity at the node denoted as "ff" in Figure **2**.

Bouzidi *et al*. [25] presented a simpler boundary condition based on the bounce-back for the wall located at arbitrary position. In their work, both linear scheme and the quadratic schemes were given to obtain $f_{\bar{\alpha}}(\boldsymbol{x}_f,t+\delta t)$ which is equivalent to $\tilde{f}_{\bar{\alpha}}(\boldsymbol{x}_b,t)$. The linear version was as follows

$$f_{\bar{\alpha}}(\boldsymbol{x}_f,t+\delta t)=\frac{1}{2\Delta}\tilde{f}_{\alpha}(\boldsymbol{x}_f,t)+\frac{2\Delta-1}{2\Delta}\tilde{f}_{\bar{\alpha}}(\boldsymbol{x}_f,t) \quad \text{for} \quad \Delta>\frac{1}{2} \qquad (17a)$$

$$f_{\bar{\alpha}}(\boldsymbol{x}_f,t+\delta t)=2\Delta\tilde{f}_{\alpha}(\boldsymbol{x}_f,t)+(1-2\Delta)\tilde{f}_{\alpha}(\boldsymbol{x}_f-\boldsymbol{e}_{\alpha}\delta t,t) \quad \text{for} \quad \Delta<\frac{1}{2} \qquad (17b)$$

In the above, we note that $\boldsymbol{x}_f-\boldsymbol{e}_{\alpha}\delta t$ is at the ff node in Figure **2**.

The above three boundary condition treatments all have second-order accuracy for curved boundary. The difference is that the first two need to construct a fictitious fluid point inside the solid wall, and perform a collision step at that node, while the scheme of Bouzidi *et al* only requires the known values of f_{α} on the fluid side and no additional collision is required. It is emphasized that all three methods need to treat the boundary condition separately for $\Delta\leq 0.5$ and $\Delta>0.5$.

In this paper, a unified scheme for curved boundary condition is presented, and tested along with those given by FH [23] and Bouzidi *et al*. [25] for several fluid flow problems: 2-D channel flow with constant pressure gradient, the Stokes first problem, and uniform flow over a column of circular cylinder. Finally the results of flow over an oscillation plate are given.

2. THE PROPOSED SOLID BOUNDARY CONDITION

A single interpolation is used for both $\Delta\leq 0.5$ and $\Delta>0.5$ in the proposed scheme. In this scheme, all the variables are in the same time t. Referring to Figure **2**, after the streaming step, $f_{\bar{\alpha}}(\boldsymbol{x}_f)$ for ($\bar{\alpha}$=4 in this example) is needed while $f_{\alpha}(\boldsymbol{x}_b)$ and $f_{\alpha}(\boldsymbol{x}_f)$ are known. Using a linear interpolation, $f_{\alpha}(\boldsymbol{x}_w)$ (for α=8) can be easily found as:

$$f_{\alpha}(\boldsymbol{x}_w)=f_{\alpha}(\boldsymbol{x}_f)+\Delta[f_{\alpha}(\boldsymbol{x}_b)-f_{\alpha}(\boldsymbol{x}_f)] \qquad (18)$$

To ensure the no-slip condition ($\boldsymbol{u}_w=0$) on the wall, considering the momentum balance in the direction of $\boldsymbol{e}_{\alpha}$, we set

$$f_{\bar{\alpha}}(\boldsymbol{x}_w)=f_{\alpha}(\boldsymbol{x}_w) \qquad (19)$$

Using $f_{\bar{\alpha}}(\boldsymbol{x}_w)$ and $f_{\bar{\alpha}}(\boldsymbol{x}_f+\boldsymbol{e}_{\bar{\alpha}}\delta t)$, we can obtain $f_{\bar{\alpha}}(\boldsymbol{x}_f)$ using a linear interpolation:

$$f_{\bar{\alpha}}(\boldsymbol{x}_f)=f_{\bar{\alpha}}(\boldsymbol{x}_w)+\frac{\Delta}{1+\Delta}[f_{\bar{\alpha}}(\boldsymbol{x}_f+\boldsymbol{e}_{\bar{\alpha}}\delta t)-f_{\bar{\alpha}}(\boldsymbol{x}_w)] \qquad (20)$$

This simple, unified formula for the boundary condition is valid for both $\Delta\geq 0.5$ and $\Delta<0.5$. For second order treatment, Eq. (18) is replaced by:

$$f_\alpha(\boldsymbol{x}_w) = f_\alpha(\boldsymbol{x}_f) + \Delta[f_\alpha(\boldsymbol{x}_b) - f_\alpha(\boldsymbol{x}_f)] + \Delta(\Delta-1)\frac{f_\alpha(\boldsymbol{x}_b) - 2f_\alpha(\boldsymbol{x}_f) + f_\alpha(\boldsymbol{x}_f + \boldsymbol{e}_{\bar{\alpha}}\delta t)}{2} \quad (21)$$

and Eq. (20) is replaced by:

$$f_{\bar{\alpha}}(\boldsymbol{x}_f) = f_{\bar{\alpha}}(\boldsymbol{x}_w) + \frac{\Delta}{1+\Delta}[f_{\bar{\alpha}}(\boldsymbol{x}_f + \boldsymbol{e}_{\bar{\alpha}}\delta t) - f_{\bar{\alpha}}(\boldsymbol{x}_w)] - \left[\frac{f_{\bar{\alpha}}(\boldsymbol{x}_f + 2\boldsymbol{e}_{\bar{\alpha}}\delta t)}{(2+\Delta)/\Delta} - \frac{f_{\bar{\alpha}}(\boldsymbol{x}_f + \boldsymbol{e}_{\bar{\alpha}}\delta t)}{(1+\Delta)/\Delta} + \frac{\Delta f_{\bar{\alpha}}(\boldsymbol{x}_w)}{(2+\Delta)(1+\Delta)}\right] \quad (22)$$

For non-zero wall velocity, $\boldsymbol{u}_w$, it can be easily incorporated into the unified formula by adding an additional momentum to $f_{\bar{\alpha}}(\boldsymbol{x}_w)$ in Eq. (19)

$$f_{\bar{\alpha}}(\boldsymbol{x}_w) = f_\alpha(\boldsymbol{x}_w) + 2w_\alpha\rho_w\frac{3}{c^2}\boldsymbol{e}_\alpha\cdot\boldsymbol{u}_w \quad (23)$$

where ρ_w can be obtained by using suitable extrapolation from the nearby fluid nodes. To avoid computational instability, we simply set $\rho = \rho(\boldsymbol{x}_f)$ since we are dealing with nearly incompressible flows.

3. COMPUTATIONAL ASSESSMENT

For the proposed boundary condition treatment to be useful, several issues need to be addressed: spatial and temporal accuracy, ability to handle geometric singularity, and flexibility to handle complex geometry. Pressure driven channel flow and Stokes first problem are used to test the accuracy of the proposed scheme. The flow over a column of circular cylinders is the case used to assess the impact of the boundary treatment on the accuracy of the flow field around a curved boundary. The flow over an oscillating zero-thickness plate is used to test the continuity in the boundary treatment.

3.1 Pressure Driven Channel Flows

The grid structure for the 2-D channel computation is shown in Figure 4. The constant pressure gradient ∇p along the *x*-direction is applied as a body force, which is added after the collision step [22]:

$$\tilde{f}_\alpha(x_i,t) = \tilde{f}_\alpha(x_i,t) - w_\alpha\frac{3}{c^2}\frac{dp}{dx}\boldsymbol{e}_\alpha\cdot\hat{x} \quad (24)$$

where $\hat{x}$ is the unit vector along the *x*-direction. At steady state, the exact solution for the *x*-velocity profile is given by

$$u_{exact}(y) = -\frac{1}{2}\frac{dp}{dx}\frac{H^2}{\rho\nu}(\eta^2-\eta) \quad (25)$$

where $H = N_y\text{-}3+2\Delta$ and $\eta = y/H = (j\text{-}2+\Delta)/H$. To assess the computational error of the LBE solution of the velocity, $u_{LBE}(y)$, the following relative L_2-norm error is defined

$$E_2 = \frac{\{\int_0^H [u_{LBE}(y) - u_{exact}(y)]^2 dy\}^{1/2}}{[\int_0^H u_{exact}^2(y)dy]^{1/2}} \quad (26)$$

In the LBE, $\delta t = \delta x = \delta y = 1$. Using the channel height $H = N_y\text{-}3+2\Delta$, the dimensionless grid size (or grid resolution) is H^{-1}.

The periodic boundary condition is used at the left and right boundary of computational domain. At the lower and upper wall, three wall boundary conditions are used: FH, Bouzidi *et al*, and the present scheme for the whole range of $0 \le \Delta \le 1$. For the computations reported here, we use $\nabla p = 10^{-8}$, $\tau = 0.51$ with double precision.

The wall slip velocity $u_w = u_x(y=0)$ is evaluated using a second order extrapolation based on $u_x(y=\Delta)$, $u_x(y=1+\Delta)$ and $u_x(y=2+\Delta)$. Here we suppose that the velocity profile of the solution is parabolic so that this second order extrapolation is adequate. Since the true wall velocity in the pressure driven channel flow is exactly zero, the wall slip velocity $\boldsymbol{u}_w$ provides a measure of the accuracy for the treatment of the wall velocity. Figure 5 shows the dependence of wall slip velocity to the H (or the grid resolution H^{-1}). Here u_w is normalized by the centerline velocity

$$u_{max} = -\frac{H^2}{8\rho\nu}\frac{dp}{dx}. \quad (27)$$

The second-order convergence of u_w with increasing H is observed clearly in the Figure 4 for $\Delta = 0.01$, 0.5, and 0.99. It is worth noting that although both the present linear and quadratic interpolations show second-order convergence, the magnitude of error of the quadratic form is much smaller.

Figure 6 shows the dependence of the relative L_2-norm error on the channel height H for $\Delta = 0.01$, 0.5, and 0.99. The second-order accuracy is clearly demonstrated in the range of H investigated. It has been well established that the accuracy of the LBE method for the interior field is of second order. The fact that the overall accuracy is of second order in the present case means that the accuracy in the boundary condition is at least of second order. This is entirely consistent with the results shown in Figure 5 which shows the local convergence ($y=0$).

While the wall slip velocity $\boldsymbol{u}_w$ can be viewed as an error in the approximate treatment for the boundary condition for the distribution function, it can also be viewed as resulting from the error in locating the wall in the LBE solution. As shown in Fig.2, the bottom wall is supposed to be at a distance of Δ below the j=2 grid line. The LBE solution, however, sees the wall at a distance of Δ' below the j=2 grid. Using a 3rd order polynomial and the velocity values at j=2, 3, 4 and 5 to fit the velocity profile near the wall, it is found that the coefficient for the cubic power term is 0; hence a

parabolic profile is an exact fit. Using the parabolic fit, the wall position Δ' can be determined. The difference (Δ'-Δ) can be used as a measure of geometric accuracy in the LBE solution. Figure 7 shows the (Δ'-Δ) as a function of 1/H for Δ =0.01, 0.5, and 0.99 using the present linear scheme. Although graphically not obvious, (Δ'-Δ)~-1/100H^{-1} for Δ=0.01. Hence (Δ'-Δ) is proportional to H^{-1} to the leading order. This asymptotic linear relationship holds also for other values of τ. With the linear scheme of Bouzidi *et al*, the linear relationship is also observed and the results for τ=0.51 are very close to that shown in Figure 7. Hence the non-dimensional geometric error scales with H^{-2} and $H'(\Delta'-\Delta)$ remains a constant.

As the wall location is altered, the channel height is also modified to $H'=H+2(\Delta'-\Delta)$. Thus the LBE solution actually sets up the following parabolic velocity profile:

$$u'_{exact}(y') = -\frac{1}{2\rho\nu}\frac{dp}{dx}(y'^2 - H'y') \qquad (28)$$

It is thus instructive to compare the LBE solution with the above modified exact velocity profile using the following L_2-norm error ,

$$E'_2 = \frac{1}{H'}\{\int_0^{H'}[u_{LBE}(y) - u'_{exact}(y')]^2 dy'\}^{1/2} \qquad (29)$$

Figure 8 shows E'_2 as a function of H for Δ=0.01, 0.5, and 0.99. Basically, E'_2 has reached the machine error.

With the modified exact velocity profile $u'_{exact}(y')$, the slip velocity can be calculated as

$$u_w \sim u'_{exact}(y' = \Delta' - \Delta)$$
$$= \frac{1}{2\rho\nu}\frac{dp}{dx}[H'(\Delta'-\Delta) - (\Delta'-\Delta)^2] \qquad (30)$$

Closer examination of the actual values of u_w as a function of H reveals that, for a given set of (τ, dp/dx, Δ), u_w does not vary with H. Hence,

$$u_w = \frac{1}{2\rho\nu}\frac{dp}{dx}B$$

where the coefficient B is a function of (τ, dp/dx, Δ). This makes the presentation for the slip velocity much easier since one set of H is sufficient. Figure 9 shows the slip wall velocity as a function of Δ using the present linear scheme and Bouzidi et al.'s linear scheme for τ =0.502, 0.51, 0.6 and 0.8 while the value of $\frac{1}{\nu}\frac{dp}{dx}$ is fixed. Again, the linear version of these two schemes perform have very similar characteristics in terms of accuracy.

It is further noticed that the largest magnitude of the slip velocity occurs mainly near Δ=1. This can be attributed to the fact that the interpolation formula given by Eq. (20) has the largest error at Δ=1. Thus to reduce the wall-slip velocity, the 2nd order interpolation formula Eq. (21) and Eq. (22) may be used. Fig. 9 shows the wall-slip velocity as a function of Δ using both quadratic forms of the present scheme and Bouzidi et al's scheme for τ =0.502, 0.51 and 0.6. Note that for the present quadratic scheme, the slip velocity is amplified by a factor 100 for τ=0.502 and by a factor of 10 for τ=0.51 in order to show all curves on the same scale. For the low viscosity (τ =0.502) case, the slip velocity using Bouzidi et al's quadratic scheme is over 100 times of that using the present quadratic formula. However, it also needs to be pointed out that for $\tau \geq 0.6$, not only these two quadratic schemes perform very similarly, but also there is little difference between the linear and quadratic versions of the present scheme. Since the high Reynolds number flow is more difficult to obtain computationally, it is important to realize that quadratic form of the present scheme may result in a much larger improvement in handling the solid boundary conditions for the large eddy type of LBE simulations.

Figure 11 shows the relative error by Eq. (26) as a function of Δ with H=15 using the present, FH's, and Bouzidi *et al*.'s boundary treatments, for $0 \leq \Delta \leq 1$. in the simulation τ=0.51 and $\nabla p = -10^{-8}$. It can be seen that the present linear scheme, Bouzidi *et al*.'s linear scheme, and FH's boundary condition have the same order of error for $0 \leq \Delta \leq 1$. Bouzidi *et al*.'s quadratic form gives a large range of error for $0 \leq \Delta \leq 1$, from 10^{-7} to 10^{-2}. The present quadratic formula yields a more uniformly distributed error in the whole range of Δ. This observation agrees well with the results obtained in the analysis of wall slip velocity. It is interesting to note that the error goes down when Δ increase for the present quadratic formula, which is opposite to other boundary conditions in Figure 11. The present linear and Bouzidi *et al*.'s linear boundary condition have very similar characteristics.

Unlike the FH boundary condition, the present boundary conditions suffers no computational instability for any $0 \leq \Delta \leq 1$ and $\tau > 0.5$. Even for τ=5.0+10^{-4}, the present boundary condition gives correct converged results.

3.2 Stokes first problem: flow due to an impulsively started wall

For a wall located at y=0 that is impulsively started, an unsteady Stokes layer of thickness $O(\sqrt{\nu t})$ develops near the wall. For a fixed-grid computation, the error at small time is expected to be large due to insufficient spatial resolution. In the LBE method, this is also compounded by the use of fixed δt (=δx=δy=1). In the computation the wall velocity is set as V=0.1. Two boundary treatments are used on the wall in the computation, FH boundary condition and present boundary condition. The relaxation time τ=0.7 gives a

kinematic viscosity ν=0.0667. At t=1.0 and 10 (lattice unit), the Stokes layer thickness is about 0.26 and 0.82, respectively, and they are both less than the grid size. Hence there is not enough spatial resolution when t is small and this will typically cause spatial and temporal oscillation in the solution.

Figure 12 shows the velocity profiles at t=10, 50, and 100 (in lattice unit). When t=10, the velocity has large relative error and it becomes negative when y is larger than 4. The oscillation of velocity is not shown in the Figure 12 because its absolute value is less than 10^{-3}. Only the result of present linear boundary treatment is shown in Figure 12.

Figure 13a and Figure 13b shows the temporal variation of the relative L_2-norm error defined as

$$E_2 = \frac{\{\int_0^\infty [u_{LBE}(y,t) - u_{exact}(y,t)]^2 dy\}^{1/2}}{[\int_0^\infty u_{exact}^2(y,t) dy]^{1/2}} \qquad (31)$$

for Δ=0.01, 0.5, and 0.99. The large relative errors in the beginning are due to lack of resolution for small time. It should be emphasized that this flow at small time is difficult to deal with for any computational technique due to the singular acceleration and large spatial gradient. It is interesting to note that the present quadratic boundary condition treatment converges to the same magnitude of error while the FH and the present linear boundary formulas diverge at a different level. In such a transient flow, the computational accuracy in the near-wall region is typically dictated by the near-wall spatial resolution which must be smaller than the Stokes layer thickness in order to resolve the local flow field. In a finite difference calculation for such a flow, δt and δy can be independently chosen. If δy is not sufficiently small, further reduction in δt will not lead to improvement in accuracy. As the Stokes layer grows to a certain thickness, the spatial resolution becomes adequate and the accuracy then improves.

3.3 Steady uniform flow over a column of cylinders

For a uniform flow over a column of circular cylinders of radius r with center-to-center distance denoted by H, symmetry conditions for f_α's are imposed at y= $\pm H/2$. At the inlet, the uniform velocity, u=V, is specified using FH boundary condition. At the exit, a simple extrapolation is used,

$$f_\alpha(N_x, j) = 2 f_\alpha(N_x\text{-}1, j) - f_\alpha(N_x\text{-}2, j) \quad \text{for } \alpha\text{=}4, 5, \& 6 \qquad (32)$$

On the surface of the circular cylinder, the FH and present boundary condition are used to update the f_α's. To reduce the effect of the inlet condition, the cylinder is placed 20 radii to the left of inlet. The outlet is placed 35 radii to the right of center of cylinder. In computation τ=0.52, u_{inlet}=0.0513. The drag coefficient is calculated using momentum exchange method [26] for both solid boundary treatments at two different cylinder center position (130.0, 65.0) and (130.2, 65.0). Different positions of the cylinder center give different Δ configurations in boundary treatment.

Table 1 shows the results of drag coefficient using the FH, present linear, and present quadratic boundary condition. The present quadratic formula gives a closer value in comparison with the value of 1.248 given by Fornberg [27] for both cylinder positions. Figure 15 shows the centerline velocity variations, upstream and downstream for two kinds of boundary conditions on cylinder with the center of cylinder at (130.0,65). The present linear and FH's treatment give very similar velocity profiles in regions with sharp gradient near the front stagnation point, very similar values for the length of the separation bubble, the maximum of the separation bubble velocity, and the recovery of the wake velocity. This result is expected because the results of C_D of the two cases are very close. The present quadratic formula gives slightly different length of the separation bubble, and hence the recovery of the wake velocity.

3.4 Flow over a vertically oscillating zero-thickness flat plate

The main difference between the present unified scheme and the previous schemes is that there is no discontinuity in the distribution function when Δ changes from below 0.5 to above 0.5. To illustrate the effect of changing Δ, a uniform flow over a vertically oscillating zero-thickness flat plate is considered here. The computational domain is shown in Figure 16. The inlet, lower, upper, and outlet boundary condition are set to be the same as those for flow over a column of cylinders. There are exactly 40 grids across the plate. The leading edge of the plate is at x=50 lattice unit from the inlet. To avoid the crossing of the plate through lattice nodes, the plate is moved according to

$$y_{plate} = y_{initial} + 0.49 \cdot \sin(t/1000)$$

with $y_{initial}$ set to be at the middle of the nodes (Δ=0.5). The computation is carried out with τ=0.52, u_{inlet}=0.0083 so that Re=20 based on the length of plate. The FH, Bouzidi *et al*'s linear, and the present linear boundary treatments are used on the surface of the plate. Figure 17a and Figure 17b show the variation of drag as the plate moves. A small discontinuity in the results using FH and Bouzidi et al's treatments is observed when the plate crosses y= $y_{initial}$. On the other hand, the present treatment gives a smooth variation.

4. CONCLUDING REMARKS

In this work a second-order accurate boundary condition treatment for the lattice Boltzmann equation method is

proposed. A series of studies are conducted to systematically test the accuracy and examine the robustness of the proposed boundary condition in steady and unsteady flows involving straight and curved walls. Compared with the existing method for treating boundary condition in the lattice Boltzmann method, the presently proposed treatment has the following advantages. (i) The scheme is unified for $\Delta \geq 0.5$ and $\Delta < 0.5$ and there is no discontinuity in boundary treatment. (ii) The boundary treatment is very robust and have good computational stability characteristics. (iii) Quadratic form of the present scheme may substantially reduce wall slip velocity for low viscosity or high Reynolds number flows.

5. ACKNOWLEDGMENTS

The work reported in this paper has been partially supported by NASA Langley Research Center, with David Rudy as the project monitor. The authors thank Dr. Li-Shi Luo for many helpful discussions.

6. REFERENCES

[1] G. McNamara & G. Zanetti, Use of the Boltzmann equation to simulate lattice-gas automata, *Phys. Rev. Lett.* **61**, 2332 (1988).

[2] F. Higuera, S. Succi, & R. Benzi, Lattice gas dynamics with enhanced collisions, *Europhys. Lett.* **9**, 345 (1989).

[3] H. Chen, S. Chen, & W. H. Matthaeus, Recovery of the Navier-Stokes equations using a lattice-gas Boltzmann method, *Phys. Rev. A*. **45**, R5339-R5342 (1992).

[4] R. Benzi, S. Succi, & M. Vergassola, The lattice Boltzmann equation: Theory and applications, *Phys. Rep*. **222**, 145-197 (1992).

[5] S. Chen & G. D. Doolen, Lattice Boltzmann method for fluid flows, *Ann. Rev. Fluid Mech.* **30**, 329-364 (1998).

[6] R. Peyret & T. D. Taylor, *Computational Technique for Fluid Dynamics*, Vol. II, (Springer-Verlag, New York, 1983).

[7] C. A. J. Fletcher, *Computational Techniques for Fluid Dynamics*, Vols. I & II, (Springer-Verlag, New York, 1988).

[8] W. Shyy, *Computational Modeling for Fluid Flow and Interfacial Transport*, Corrected printing, (Elsevier, Amsterdam, 1997).

[9] P. L. Bhatnagar, E. P. Gross, & M. Krook, A model for collision processes in gases. I. Small amplitude processes in charged and neutral one-component system, *Phys. Rev. A*, **94**, 511-525 (1954).

[10] X. He & L.-S. Luo, A priori derivation of the lattice Boltzmann equation, *Phys. Rev. E* **55**, R6333-R6336 (1997).

[11] X. He & L.-S. Luo, Theory of the lattice Boltzmann equation: From Boltzmann equation to lattice Boltzmann equation, *Phys. Rev. E* **56**, 6811 (1997).

[12] D. P. Ziegler, Boundary conditions for lattice Boltzmann simulations. *J. Stat. Phys*. **71**, 1171-1177(1993).

[13] I. Ginzbourg, P. M. Alder, Boundary flow condition analysis for the three-dimensional lattice Boltzmann model, *J. Phys. II France* **4,** 191-214 (1994).

[14] S. Wolfram, Cellular automaton fluids. 1:Basic theory, J Stat Phys **45**, 471–526 (1986).

[15] P. Lavallee, J.P. Boon, A. Noullez, Boundaries in lattice gas flows, Physica D **47,** 233-240 (1991).

[16] A. J. C Ladd, Numerical simulation of particular suspensions via a discretized Boltzmann equation. Part 2. Numerical results, *J. Fluid Mech.* **271**, 311-339 (1994).

[17] D. R. Noble, S. Chen, J. G. Georgiadis, R. O. Buckius, A consistent hydrodynamic boundary condition for the lattice Boltzmann method. *Physics of Fluids* **1**, 203-209 (1995).

[18] T. Inamuro, M. Yoshino, F. Ogino, A Non-slip boundary condition for lattice Boltzmann Simulations. *Phys. Fluids* **7,** 2928-2930 (1995).

[19] R. S. Maier, R. S. Bernard, D. W. Grunau, Boundary conditions for the lattice Boltzmann methods. *Phys. Fluids* **8**,1788-1801(1996).

[20] S. Chen, D. Martinez, R. Mei, On boundary conditions in lattice Boltzmann method, *Phys. Fluids* **8**, 2527-2536 (1996).

[21] Q. Zou, X. He, On pressure and velocity boundary conditions for the lattice Boltzmann BGK model, *Phys. Fluids* **9**:1591-1598(1997).

[22] X. He, Q. Zou, L.-S. Luo, M. Dembo, Analytic solutions and analysis on non-slip boundary condition for the lattice Boltzmann BGK model. J Stat Phys **87,** 115-136 (1997).

[23] Q. Filippova and D. Hänel, Grid refinement for lattice-BGK models, *J. Comp. Phys.* **147**, 219-228 (1998).

[24] R. Mei, L.-S. Luo, W. Shyy, An accurate curved boundary treatment in the lattice Boltzmann method, *J. Comp. Phys.,* **155**, 307-330 (1999).

[25] M. Bouzidi, M. Firdaouss, and P. Lallemand, Momentum transfer of a lattice Boltzmann fluid with boundaries. *Physics of fluids*. **13**, no. 11, 3452 (2001).

[26] R. Mei, D. Yu, W. Shyy, L.-S. Luo, Force evaluation in the lattice Boltzmann method involving curved geometry. *Phys Rev E* **65**, 041203:1-041203:14 (2002).

[27] B. Fornberg, Steady incompressible flow past a row of circular cylinder, *J. Fluid Mechanics*, **225**, 655-671(1991).

Table 1 Comparison of Drag coefficient for flow over a column of cylinder at Re=100.

(x_c,y_c)	Present Linear	Present quadratic	FH	C_d, [21]
(130.0,65)	1.275	1.247	1.271	1.248
(130.2,65)	1.290	1.251	1.274	

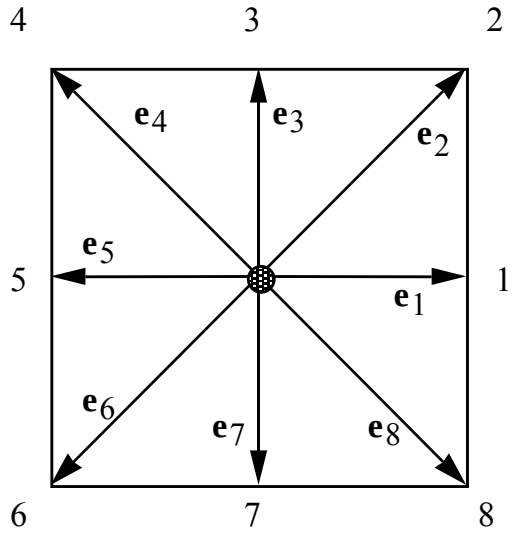

Figure 1 A 2-D, 9-velocity lattice.

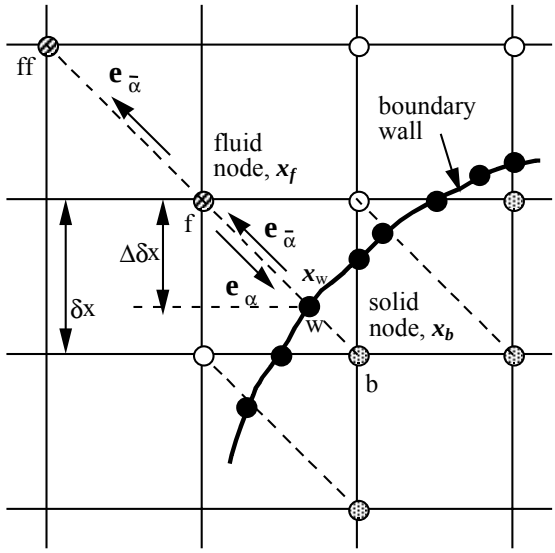

Figure 2 Layout of the regularly spaced lattices and curved wall boundary.

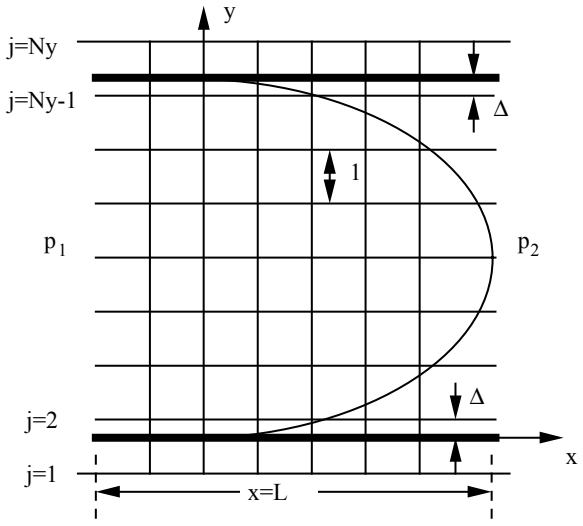

Figure 4 Lattice distribution in channel flow simulations with arbitrary Δ.

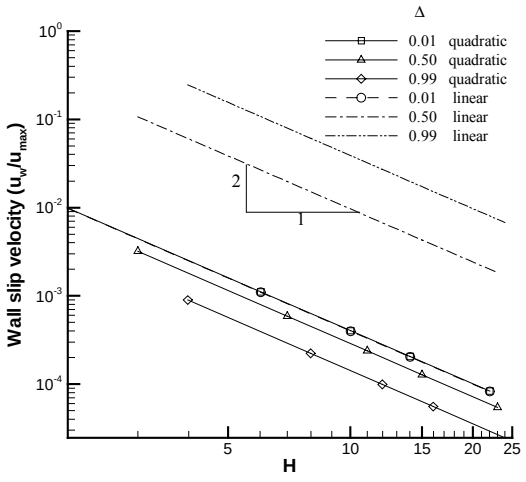

Figure 5 Quadratic convergence of the wall slip velocity using the present boundary condition in constant pressure driven channel flow.

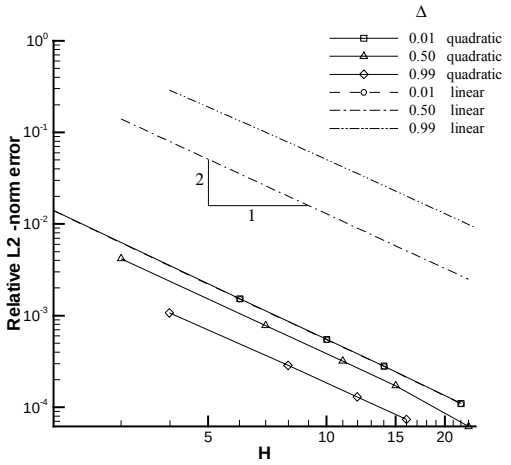

Figure 6 Dependence of relative L_2-norm error, defined in Eq. (26), on the lattice resolution H using the present boundary condition in the steady state pressure-driven channel flow.

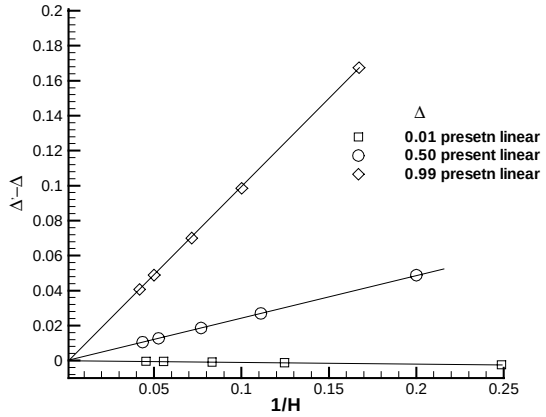

Figure 7 The variation of (Δ'-Δ) as a function of 1/H for Δ =0.01, 0.5, and 0.99 using the present linear scheme.

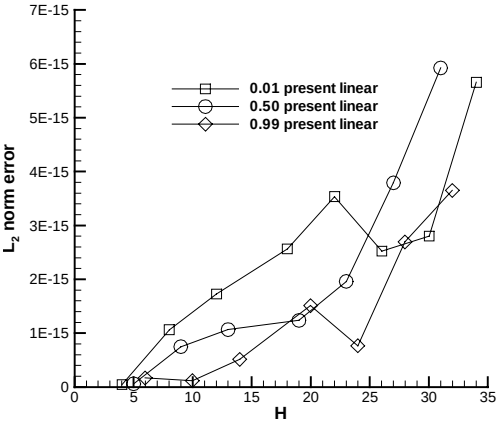

Figure 8 Dependence of relative L_2-norm error, defined in Eq. (29), on the lattice resolution H using the present boundary condition in the steady state pressure-driven channel flow.

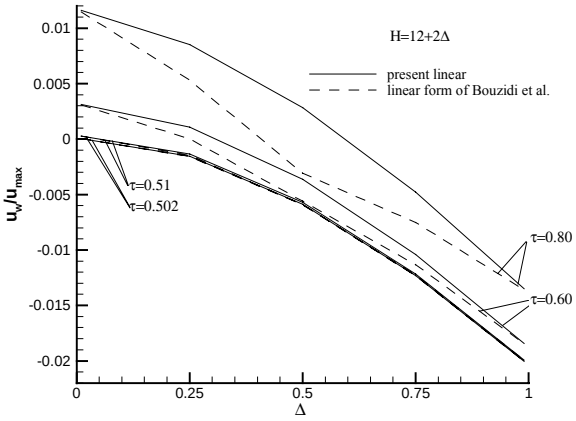

Figure 9 Slip wall velocity as a function of Δ using the present linear scheme and Bouzidi et al.'s linear scheme for τ =0.502, 0.51, 0.6 and 0.8; $\frac{1}{\nu}\frac{dp}{dx} = -3\times10^{-6}$.

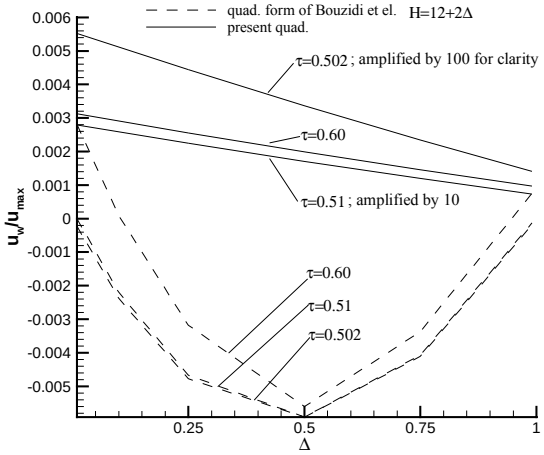

Figure 9 Slip wall velocity as a function of Δ using the present quadratic scheme and Bouzidi et al.'s quadratic scheme for τ=0.502, 0.51, 0.6 and 0.8. $\frac{1}{\nu}\frac{dp}{dx} = -3\times10^{-6}$.

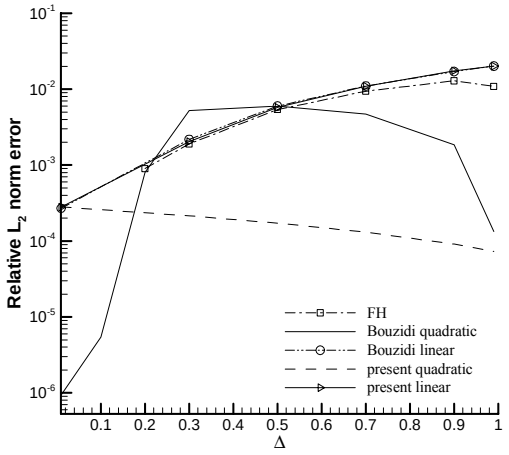

Figure 11 Relative L_2-norm error, defined in Eq. (26), as a function of Δ using different boundary treatments for steady state pressure-driven channel flow; H=12+2Δ.

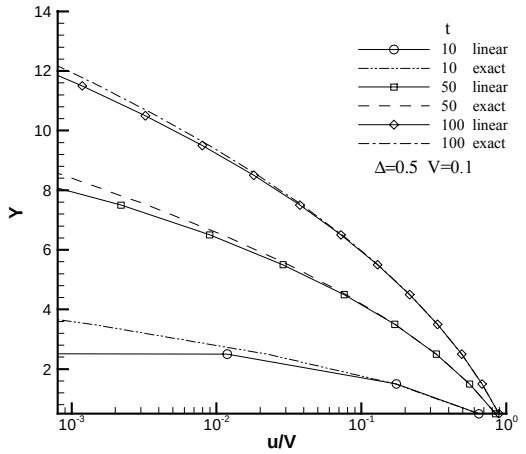

Figure 12 Velocity profiles at different times using the present linear boundary condition for an impulsively started plate (Δ= ½).

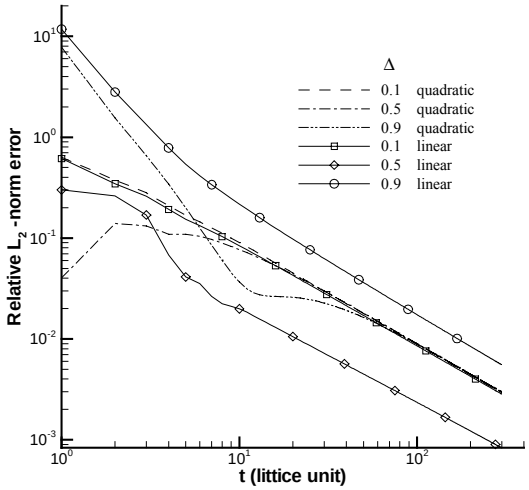

Figure 13a Relative L_2-norm error of the velocity profile $u_x(y)$ during the initial transient of the impulsively started plate with various values of Δ using the present boundary condition.

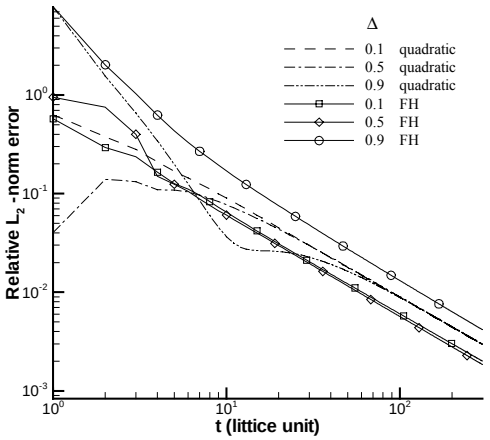

Figure 13b Relative L_2-norm error of the velocity profile $u_x(y)$ during the initial transient of the impulsively started plate with various values of Δ using the present quadratic and FH boundary conditions.

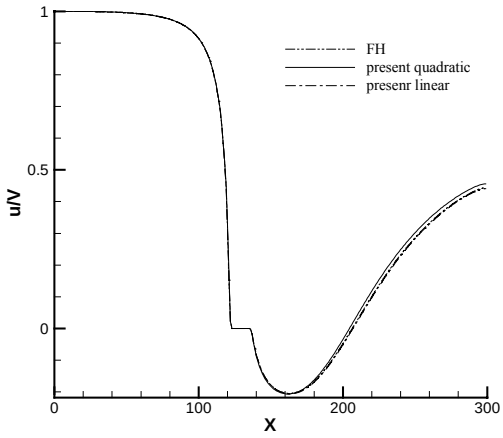

Figure 15 Centerline velocity variation for a uniform flow over a column of cylinders with FH [23], present quadratic, and present linear boundary conditions. Center of cylinder is at (130,65).

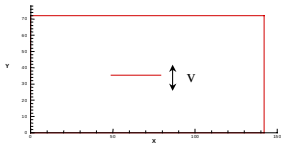

Figure 16 **C**omputational domain for flow over vertically oscillating zero-thickness plate.

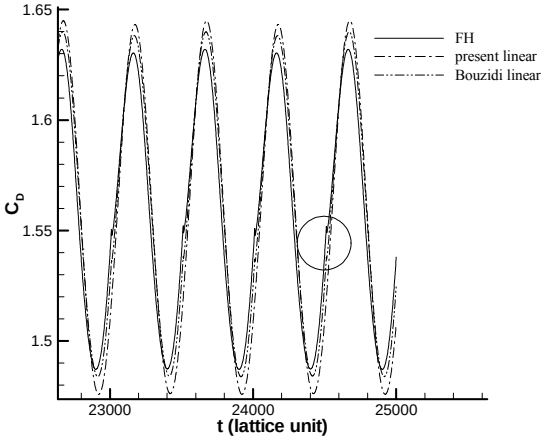

Figure 17a Drag coefficient C_D for flow over oscillating zero-thickness plate using three different boundary treatments: FH [23], Bouzidi *et al* linear scheme [25], and present linear scheme.

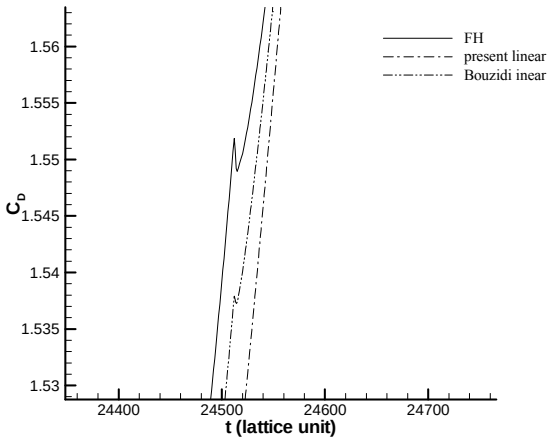

Figure 17b Enlarged view of C_D in the circled region in Figure 17a when plate crosses the middle of girds. The discontinuity in C_D is believed to be due to the discontinuity in the boundary treatment.